Design–Build–Test–Learn-Guided Engineering of a Whole-Cell Pyruvate Biosensor Based on a Transcription Factor

ACS synthetic biology

Gao, Zihan; Suarez-Diez, Maria; Candry, Pieter

https://doi.org/10.1021/acssynbio.5c00650

ACS Synthetic Biology

pubs.acs.org/synthbio Research Article

Design–Build–Test–Learn-Guided Engineering of a Whole-Cell Pyruvate Biosensor Based on a Transcription Factor

Zihan Gao, Maria Suarez-Diez, and Pieter Candry*

Cite This: ACS Synth. Biol. 2026, 15, 548–560 Read Online

ACCESS | Metrics & More | Article Recommendations | Supporting Information

ABSTRACT: Whole-cell biosensors are powerful tools for metabolite monitoring, yet challenges such as narrow dynamic range and high leaky expression limit their broader applications. Here, we present a systematic workflow based on two Design–Build–Test–Learn (DBTL) cycles to develop and optimize a transcription factor-based pyruvate biosensor in *Escherichia coli*. In the first iteration of the cycle, we constructed a biosensor that responded to intracellular pyruvate levels within the 0.05–10 mM range. In the second cycle, we implemented the design of experiments (DoE) to systematically explore combinatorial effects of promoters and ribosome-binding sites (RBSs). A first set of experiments was designed to identify factors with a significant effect on biosensor performance. The results showed that the RBS of the reporter gene significantly influenced the dynamic range by modulating basal and maximum expression, while the RBS of the transcription factor affected the signal span. The Akaike Information Criterion was used to select a model incorporating two main effects and one interaction effect. The best-performing strain exhibited an 18.54-fold increase in the dynamic range and a 37.22-fold reduction in leaky expression. Quantification of intracellular pyruvate confirmed an operational range of 1.23–6.81 μmol/g DCW. Our work demonstrates the power of DBTL cycles with statistical modeling for biosensor engineering, offering potential applications in precise metabolic regulation and screening applications.

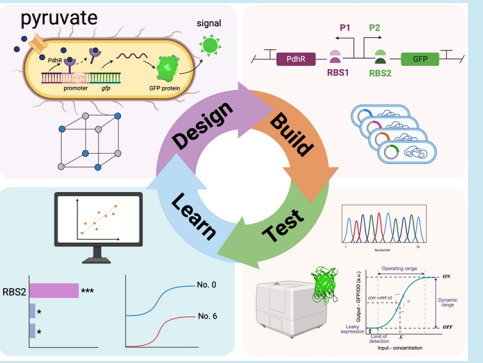

KEYWORDS: *whole-cell biosensor, DBTL cycle, transcription factor-based pyruvate biosensor, dynamic range, design of experiments, statistical modeling*

1. INTRODUCTION

Whole-cell biosensors have been drawing increasing attention over the last few decades. They couple a biological recognition element with a transducer that translates the biorecognition event into measurable signals.[1] In contrast to traditional physical and chemical sensors, whole-cell biosensors are highly sensitive, easy-to-manufacture, and cost-effective,[2,3] showing widespread applications in metabolic engineering,[4−7] disease diagnosis,[8] food contaminant detection,[9] and environmental monitoring.[10] Despite these advantages, their sensing performance often falls short of real-world detection requirements, particularly regarding restricted dynamic ranges, high leaky expression, and limit of detection.[11,12] Figure 1A conceptually illustrates these key characteristics, which often require optimization.

Recent advances in synthetic biology have provided tools to improve biosensor performance, such as promoter and ribosome-binding site (RBS) engineering for precise control of gene expression.[14,15] The performance can be optimized sequentially by tuning individual genetic factors in isolation.[4,16,17] However, the cost of constructing and testing large numbers of genetic variants limits our ability to identify high-performance designs.[7] Combinatorial optimization of circuits based on simultaneous optimization of multiple genetic factors facilitates biosensor development.[18]

Design of experiments (DoE) procedures are essential to probe multidimensional experimental space with a minimum number of experimental runs (Figure 1B). Statistical model-based DoE procedures have been widely used to simultaneously optimize multiple factors in biological processes, including optimization of conditions,[19] design of the bioprocess,[20] or metabolic pathway regulation.[21] The process often starts by considering two levels (low and high) per factor. The experimental results are summarized in a polynomial model in which main effects (MEs) describe how the response changes when each factor is varied individually, while two-factor interaction (2FI) and multiple-factor interaction (xFI) describe the effect of the simultaneous change of two or more factors. The significance of each model parameter can then be evaluated using the analysis of variance (ANOVA). Exploring

Received: September 1, 2025
Revised: December 22, 2025
Accepted: January 8, 2026
Published: February 8, 2026

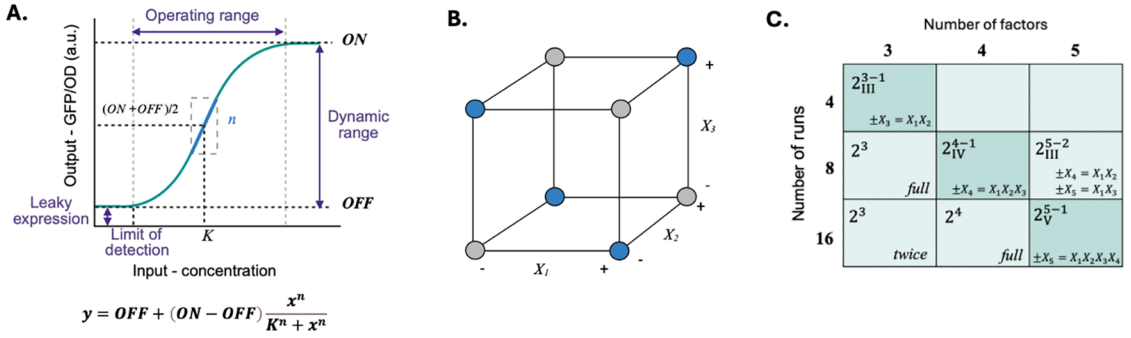

Figure 1. Overview of biosensor response modeling and design of experiments (DoE) strategy. (A) Dose−response model is fitted to a Hill's equation. *Dynamic range* is defined as the ratio of maximum output signal (ON state) to the minimum output signal (OFF state). *Leaky expression* refers to the output level in the absence of an input signal (OFF state). The *limit of detection* (LOD) is the lowest concentration of input, which can be detected from background response. *Operating range* is the detectable concentration range of target concentration. These characteristics are commonly used to define the response of the biosensor. (B) Schematic representation of the design space in a factorial DoE framework. (C) Fractional factorial design matrix illustrating the trade-off between the number of factors, resolution, and experimental runs. Higher-resolution designs ensure the identification of main effects (MEs) and interactions at the cost of increased experimental workload. The resolution (e.g., III, IV, V) characterizes the aliasing structure of the design and indicates the degree to which MEs and interaction terms are confounded. Resolution III designs require fewer experiments but cannot reliably distinguish MEs from two-factor interactions (2FI). Resolution IV designs allow the identification of MEs while confounding 2FI with one another. Resolution V designs allow identification of MEs and 2FI while confounding three-factor interactions (3FI) among each other.[13]

all possible combinations of factor levels can result in a large experimental burden as 2^n experiments are needed for n factors and 2 levels. Instead, fractional factorial design is an efficient screening method to identify MEs with less experiments[22] (Figure 1C). Different factorial designs exist depending on the number of experiments but may result in confounded 2FI and xFI.[18] For instance, resolution IV designs can identify MEs but confound 2FI among each other. Consequently, this approach can indicate if 2FI are important but cannot distinguish which 2FI is most important. Although 2FI are confounded, these designs allow weighing their importance compared to the individual effects.[23] Additionally, model selection criteria such as the Akaike Information Criterion (AIC) can further support model evaluation and refinement.[24] In this study, we set out to test whether integrating DoE strategies with DBTL cycles could enable the efficient and systematic optimization of biosensor performance.

Here, we applied a Design−Build−Test−Learn (DBTL) cycle to guide the engineering of whole-cell biosensors, which offers a systematic framework to iterate the steps of genetic circuits design, circuit construction, high-throughput screening, and statistical modeling.[25−27] This approach was applied to pyruvate biosensors as a case study, as pyruvate is an important node linking glycolysis to the tricarboxylic acid (TCA) cycle[28] as well as toward the synthesis of amino acids such as threonine, arginine, and succinate.[29,30] Traditional analytical methods for pyruvate (e.g., HPLC, fluorimetric assays) are cumbersome and incapable of quantitative monitoring in living cells.[25,31] Pyruvate biosensors would allow measuring intracellular pyruvate levels and dynamically control bioprocesses.[7,32,33] Building on these advancements, we implemented a two-cycle DBTL workflow to engineer a pyruvate-responsive biosensor in *Escherichia coli*. In the first cycle, we constructed a PdhR-based pyruvate biosensor in the *E. coli* Δ*pdhR* strain. Then, in the second cycle, a resolution IV fractional factorial design was used to explore the effect of two promoters and two RBSs on biosensor performance. A statistical model then supported the selection of the optimized biosensor design, which was used to validate the relationship between intracellular pyruvate concentration and biosensor output. Overall, the statistical DoE methodology proved to be a powerful and efficient strategy for enhancing biosensor performance and establishes a platform for intracellular pyruvate monitoring.

2. RESULTS

To systematically develop and optimize the performance of a whole-cell pyruvate biosensor, we implemented two rounds of the DBTL cycle in *E. coli* Δ*pdhR*. The following sections describe the construction, testing, and optimization steps. Figure 2 illustrates the workflows of both DBTL cycles. In the first cycle, a PdhR-based genetic circuit was constructed to detect intracellular pyruvate within 0.05−10 mM. In the second cycle, a fractional factorial design guided optimization, leading to an improved biosensor with enhanced 18.54-fold dynamic range.

2.1. DBT Cycle 1: Construction of a PdhR-Based Pyruvate Biosensor

In the first round of DBT, we constructed a PdhR-based biosensor for detecting intracellular pyruvate in *E. coli* Δ*pdhR*.

2.1.1. Design: Pyruvate-Responsive Genetic Circuit. As a first step, the biosensor design leveraged PdhR as a pyruvate-sensing repressor to control *sfGFP* expression as a function of the intracellular pyruvate concentration (Figure 3A). The gene circuit consisted of *pdhR* from *E. coli* MG1655 under the control of the constitutive promoter P_{J115}. Then, the reporter gene *sfGFP* was selected for its enhanced folding efficiency and brightness, enabling accurate and robust quantification of gene expression in an aerobic environment. *sfGFP* expression was driven by the Ppdh promoter, which contains the PdhR binding site. Both genes were equipped with ribosome-binding sites (RBS30) to ensure the proper translation efficiency (Figure 3B).

2.1.2. Build: DNA Assembly and Transformation. In the build stage, the genetic circuit was assembled by HiFi DNA assembly into the pUC19 plasmid. Since the *E. coli* genome contains the *pdhR* gene, we chose to use a pdhR-knockout strain to eliminate the influence of genomic *pdhR* on the experiment. Transformed strains were verified by colony PCR and Sanger sequencing.

https://doi.org/10.1021/acssynbio.5c00650
ACS Synth. Biol. 2026, 15, 548−560

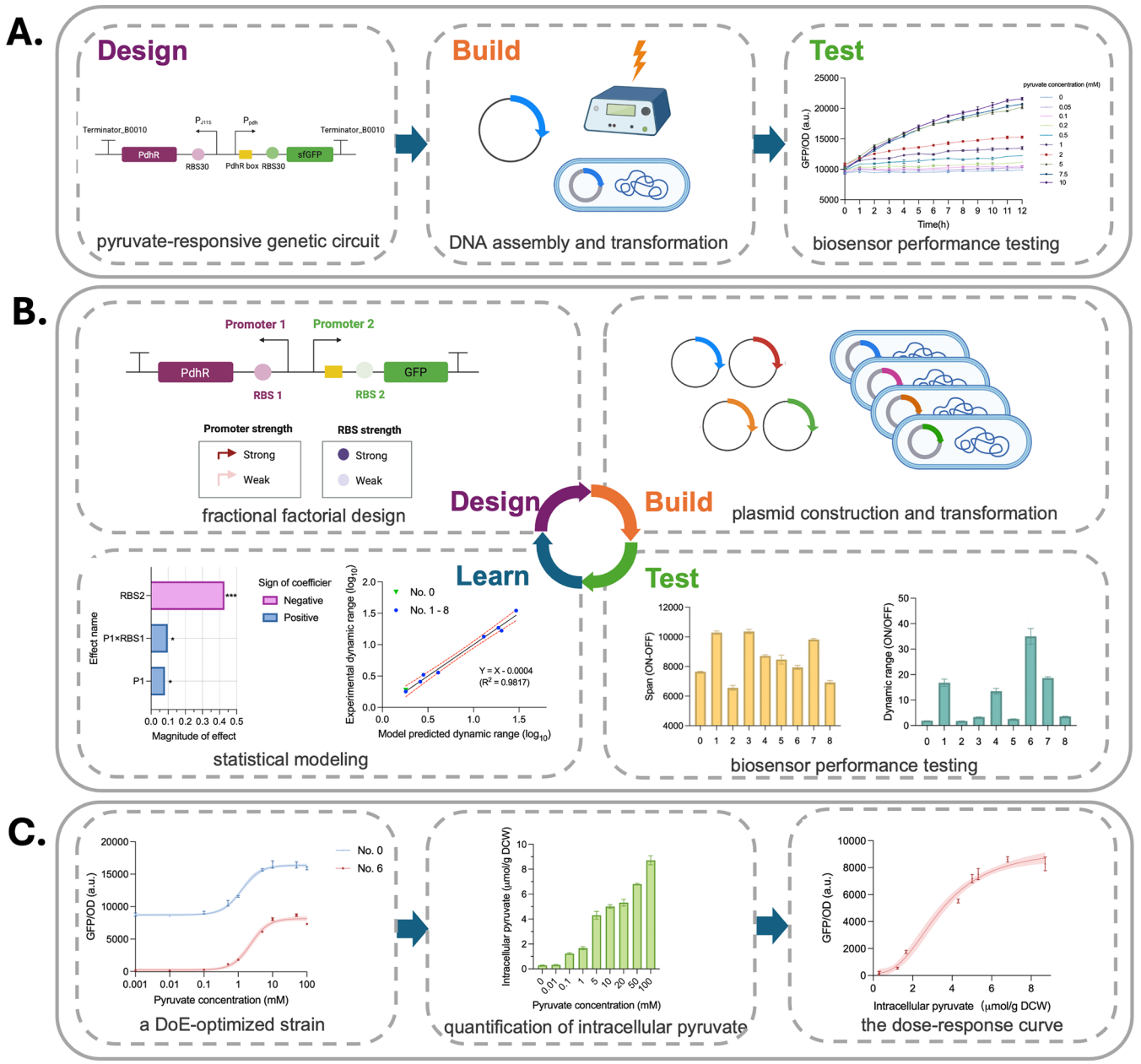

Figure 2. Overview of two rounds of DBTL cycle for the development and optimization of the pyruvate biosensor. (A) In the first DBT cycle, we designed a PdhR-based genetic circuit to detect intracellular pyruvate concentration. The genetic circuit was assembled into a plasmid and transformed into *E. coli* Δ*pdhR*, and biosensor performance was evaluated. (B) In the second DBTL cycle, a fractional factorial Design was used to combine two promoters and two RBSs. These designs were then Built by transforming assembled plasmids into *E. coli* Δ*pdhR*. The performance of the transformed strains was Tested by fitting biosensor outputs to a Hill curve to evaluate the biosensors' span (ON−OFF) and dynamic range (ON/OFF). In the Learn stage, statistical modeling revealed main effects influencing the dynamic range, guiding the selection of an optimized strain. (C) Finally, the optimized strain was validated to show improved performance, and the response was linked to intracellular pyruvate concentrations.

2.1.3. Test: Biosensor Performance Testing. In the presence of 0.05−10 mM pyruvate, the relative fluorescence intensity of the biosensor increased with rising pyruvate concentrations (Figure 3C). This indicated that pyruvate effectively activated the biosensor. The 6 h time point was selected as it provided a distinguishable GFP/OD signal across pyruvate concentrations while also minimizing the need for extended incubation. At this time, the biosensor exhibited a linear response within the 0.1−5 mM range (R^2 = 0.97), which supported its application for quantitative pyruvate detection within this range (Figure 3D). Last, based on the significant difference in the GFP/OD signal between 0.05 mM and 0 mM pyruvate (P < 0.001), the limit of detection was placed at 0.05 mM (Figure 3E).

2.2. Design and Validation of a PdhR-Regulated Hybrid Promoter

To assess the modularity and functionality of regulatory factors within the biosensor framework, we designed a hybrid promoter, $P_{J106\_PdhR\ box}$, and used this to control *sfGFP* expression (Figure 4A). To further investigate the regulatory role of PdhR, we compared GFP in the PdhR-knockout strain to that in a strain containing PdhR (Figure 4B). If the hybrid

https://doi.org/10.1021/acssynbio.5c00650
ACS Synth. Biol. 2026, 15, 548−560

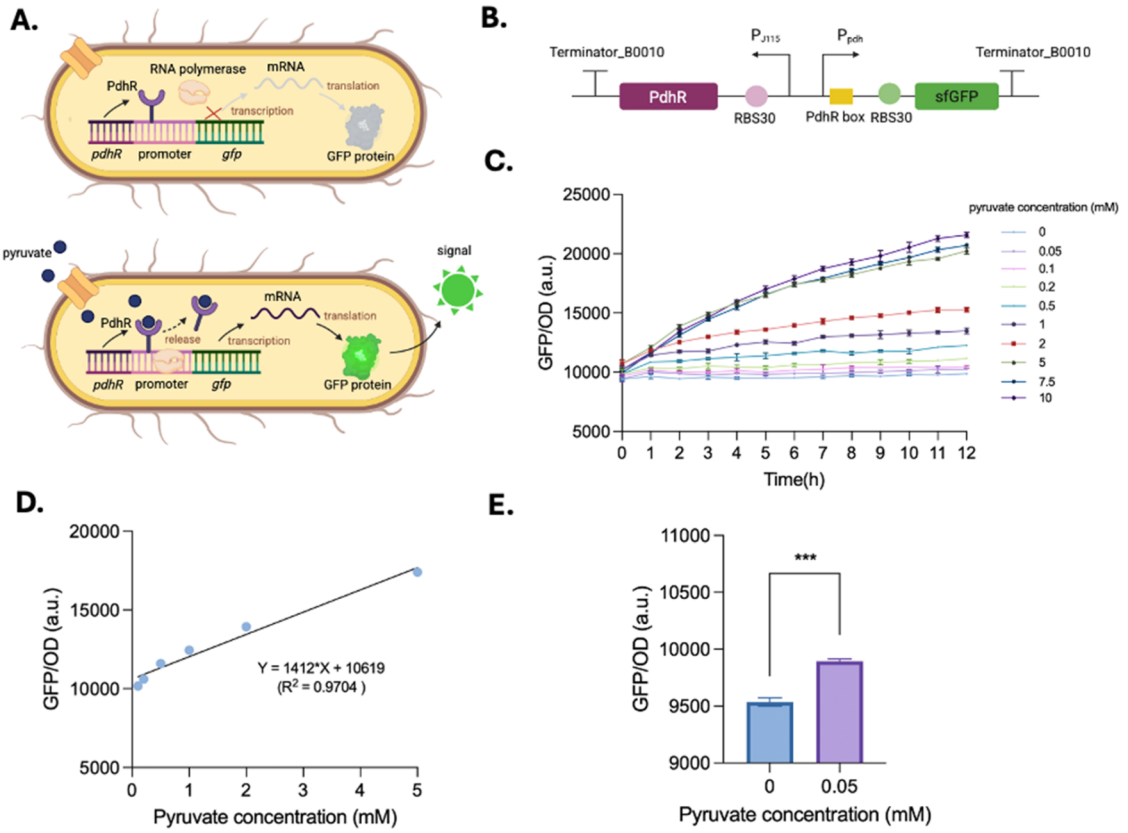

Figure 3. Construction and characterization of a PdhR-based pyruvate biosensor. (A) Schematic representation of the PdhR-based biosensor. PdhR belongs to the GntR family of transcription factors, consisting of an N-terminal helix−turn−helix (HTH) DNA-binding domain for DNA recognition and a C-terminal effector-binding domain involved in ligand sensing and oligomerization.[34] In the absence of pyruvate, the HTH motifs of PdhR enable high-affinity binding to the PdhR operator (PdhR box) on the promoter of *sfGFP*, repressing its transcription and preventing *sfGFP* expression.[35] When pyruvate is present, it binds to the C-terminal domain of PdhR and induces a conformational change. This structural rearrangement propagates to the N-terminal HTH domains, altering their relative spacing and orientation and consequently reducing the DNA-binding affinity of PdhR.[36] As a result, PdhR dissociates from its cognate promoter, allowing RNA polymerase to initiate *sfGFP* transcription and translation. Within a certain range, the fluorescence intensity of sfGFP reflects the intracellular concentration of pyruvate. (B) Genetic circuit of PdhR-based biosensor. A constitutive promoter P_{J105} and RBS30 control the expression of PdhR, which binds to the PdhR box in P_{pdh}. (C) Dose dependence of biosensor response to pyruvate. Measurements indicate mean and standard deviation of triplicate experiments. (D) Linear relationship between pyruvate concentration and GFP/OD at 6 h. (E) Statistically significant response to 0.05 mM pyruvate at 6 h, ***$P < 0.001$.

promoter functions as intended, GFP transcription would be repressed by PdhR, leading to a higher GFP signal in a non-PdhR strain compared to a PdhR-containing strain. At 0 h, the strain without PdhR showed significantly higher GFP expression than the strain with PdhR (Figure 4C; $P < 0.001$). This indicated the inhibitory effect of PdhR already existed during the LB growth stage. When the strains were then cultivated in M9 medium containing 10 mM pyruvate, both groups showed increased GFP/OD values compared to 0 h, but the strain without PdhR remained significantly higher than the strain with PdhR ($P < 0.001$). Additionally, the strain with PdhR demonstrated a significant increase in GFP/OD following pyruvate treatment, confirming that pyruvate can activate the biosensor by relieving PdhR-regulated repression. These results illustrate that PdhR can inhibit the transcription of the hybrid promoter $P_{J106\_PdhR\ box}$. This validation step ensured that the engineered promoter retained functionality for the following combinatorial design experiments.

2.3. DBTL Cycle 2: DoE to Optimize Performance

To optimize the performance of the biosensor, we aimed to simultaneously maximize its dynamic range (ON/OFF), minimize background expression (OFF), and increase span (ON−OFF). This could be achieved through systematic combinations of promoters and RBSs at different strengths guided by a fractional factorial design. The goal of our work was to develop a statistical model that can screen the main factors and interactions, providing valuable insights for future efforts in biosensor construction, optimization, and fine-tuning.

2.3.1. Design: Fractional Factorial Design. In our study, we conducted a round of DoE to optimize the performance of the PdhR-based biosensor. We focused on four key factors: (1) P1: the promoter of *pdhR*, which regulates the transcription of *pdhR*, (2) RBS1: the ribosome-binding site of *pdhR*, which modulates the translation of *pdhR*, (3) P2: the promoter of *sfGFP*, which controls the transcription of reporter gene, and (4) RBS2: the ribosome-binding site of *sfGFP*, which determines the translation level of *sfGFP*. Each factor was assigned discrete levels: the low level was coded as −1 and the high level as 1. Given the size of the screened library, a total of 16 combinations would be needed to fully explore the combinatorial space. We selected a fractional factorial design to reduce the experimental effort. Here, a resolution IV design was implemented, as it can identify the main effects and whether two-factor interactions affect biosensor performance.

https://doi.org/10.1021/acssynbio.5c00650
ACS Synth. Biol. 2026, 15, 548−560

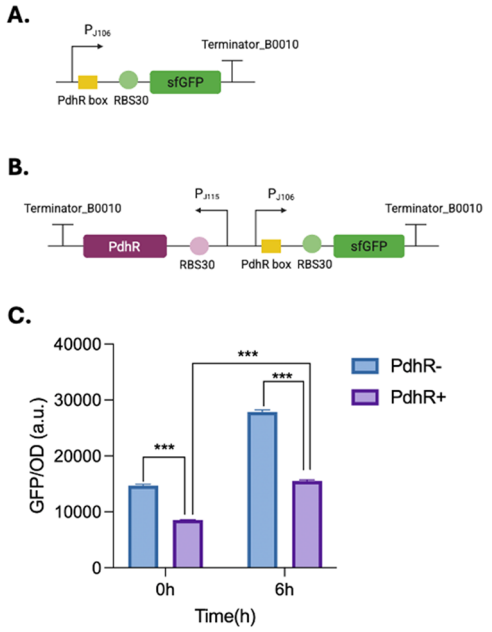

Figure 4. Construction and functional validation of a hybrid promoter. (A) Schematic diagram of the integration of the PdhR box into constitutive promoter P_{J106}. (B) Schematic diagram of the hybrid promoter in strain with PdhR. (C) Strength of the hybrid promoter in strains with (purple column) or without PdhR (blue column) at 0 and 6 h, ***$P < 0.001$.

In our case, a resolution IV design with 4 factors resulted in $2^{4-1} = 8$ experiments (strains), as illustrated in Figure 1C.

2.3.2. Build: Plasmid Construction and Transformation. We assembled eight genetic circuits with different promoters and RBSs, driven by strong (1) or weak (−1). No. 0 was regarded as control, with P2 in this strain being P_{pdh} from the *E. coli* genome (Table 1 and S5).

2.3.3. Test: Biosensor Performance Testing. We assessed the performance of pyruvate biosensors by measuring GFP/OD at various pyruvate concentrations and fitting the data to a Hill curve. The OFF state corresponds to the minimum expression of the biosensor, while the ON state represents the maximum expression. The biosensors' span and dynamic range were calculated (Table 1).

2.3.4. Learn: Statistical Modeling. The tested strains varied in performance in both the span and dynamic range. The span varied up to 1.36-fold (Figure 5A). ANOVA analysis indicated that effects of P1, P2, and RBS2 were insignificant ($P > 0.05$). RBS1, on the other hand, had a significant negative effect on the span ($P = 0.011$, Figure 5B,C and Table S6). Dynamic ranges varied from 1.88 ± 0.01 to 34.86 ± 3.10 (a.u.) (Figure 5D). ANOVA analysis showed that RBS2 had a significant negative effect on the dynamic range ($P = 0.0066$), whereas the effects of other factors were not significant ($P > 0.05$) (Figure 5E,F and Table S6). The regression models for span and dynamic range exhibited a good fit to the experimental data, with adjusted R^2 values of 0.85 and 0.86, and P values of 0.038 and 0.035, respectively, indicating statistical significance and joint contributions of the selected factors. These coefficients in the model indicated that RBS1 played a crucial role in modulating the span, while RBS2 strongly influenced the dynamic range. Both showed a negative effect.

Table 1. Fractional Factorial Design to Screen Factors That Affect Biosensor Performance[a]

no.	P1	RBS1	P2	RBS2	OFF (a.u.)	ON (a.u.)	span (ON−OFF)	dynamic range (ON/OFF)	OFF ($\log_{10}$)	ON ($\log_{10}$)	dynamic range ($\log_{10}$)
0	−1	1	n.a	1	8720.7 ± 24.2	16363.0 ± 25.4	7642.7 ± 26.1	1.88 ± 0.01	3.9405 ± 0.0012	4.2139 ± 0.0007	0.2733 ± 0.0011
1	−1	−1	−1	−1	654.0 ± 54.5	10937.0 ± 59.6	10283.0 ± 113.8	16.72 ± 1.42	2.8156 ± 0.0354	4.0389 ± 0.0024	1.2233 ± 0.0378
2	−1	1	−1	1	8286.7 ± 107.6	14841.0 ± 144.4	6554.3 ± 167.0	1.79 ± 0.03	3.9184 ± 0.0056	4.1715 ± 0.0042	0.2531 ± 0.0066
3	−1	−1	1	1	4495.0 ± 95.6	14857.7 ± 59.5	10362.3 ± 145.6	3.31 ± 0.08	3.6527 ± 0.0092	4.1720 ± 0.0017	0.5192 ± 0.0106
4	−1	1	1	−1	700.8 ± 58.4	9408.7 ± 33.2	8708.0 ± 82.3	13.43 ± 1.10	2.8456 ± 0.0354	3.9735 ± 0.0015	1.1279 ± 0.0363
5	1	−1	−1	1	5415.0 ± 105.3	13882.0 ± 199.9	8466.7 ± 301.0	2.56 ± 0.09	3.7336 ± 0.0085	4.1425 ± 0.0062	0.4089 ± 0.0145
6	1	1	−1	−1	234.3 ± 16.6	8168.7 ± 124.9	7934.3 ± 140.6	34.86 ± 3.10	2.3698 ± 0.0314	3.9122 ± 0.0066	1.5424 ± 0.0375
7	1	−1	1	−1	558.3 ± 12.5	10374.0 ± 65.5	9816.0 ± 76.7	18.58 ± 0.52	2.7469 ± 0.0097	4.0159 ± 0.0027	1.2691 ± 0.0122
8	1	1	1	1	2687.0 ± 33.5	9612.7 ± 129.8	6926.0 ± 124.7	3.58 ± 0.06	3.4293 ± 0.0054	3.9828 ± 0.0059	0.5536 ± 0.0068

[a]OFF and ON are the results of the fit to the Hill equation (see the Materials and Methods). The corresponding Hill coefficients are listed in Table S5. All the reported values indicate the mean of three biological replicates with ± denoting the standard deviation (SD) of three replicates. n.a. represents not applicable.

https://doi.org/10.1021/acssynbio.5c00650
ACS Synth. Biol. 2026, 15, 548−560

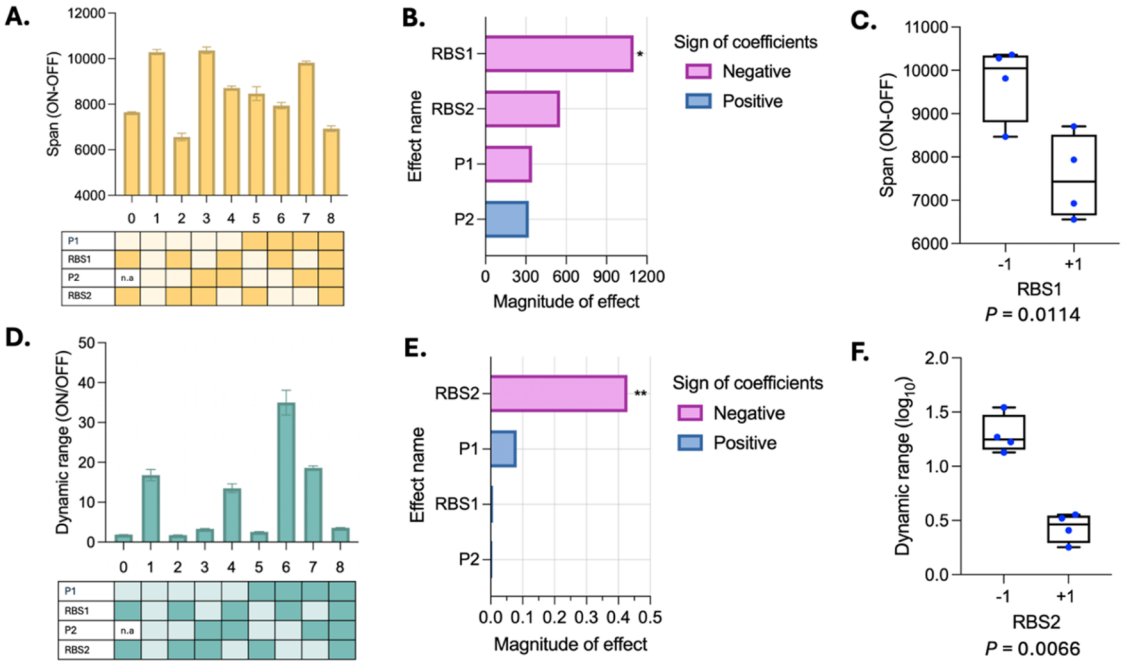

Figure 5. Screening and statistical analysis of main factors affecting biosensor performance. (A) Span of multiple tested biosensor variants. Light color indicated low level (−1) and dark color indicated high level (1). (B) Coefficients of model including main effects on span. The magnitude of effect refers to the value of the estimated coefficient from the linear mode. *P < 0.05, **P <0.01. (C) ANOVA analysis of the effect of RBS1 on span. ANOVA analysis data were obtained from the fractional factorial design. The box displays the interquartile range (IQR), with the line indicating the median, and whiskers extending to the minimum and maximum values. (D) The dynamic range of multiple tested strains. (E) Coefficients of model including main effects on the $\log_{10}$-transformed dynamic range. (F) ANOVA analysis of the effect of RBS2 on the $\log_{10}$-transformed dynamic range.

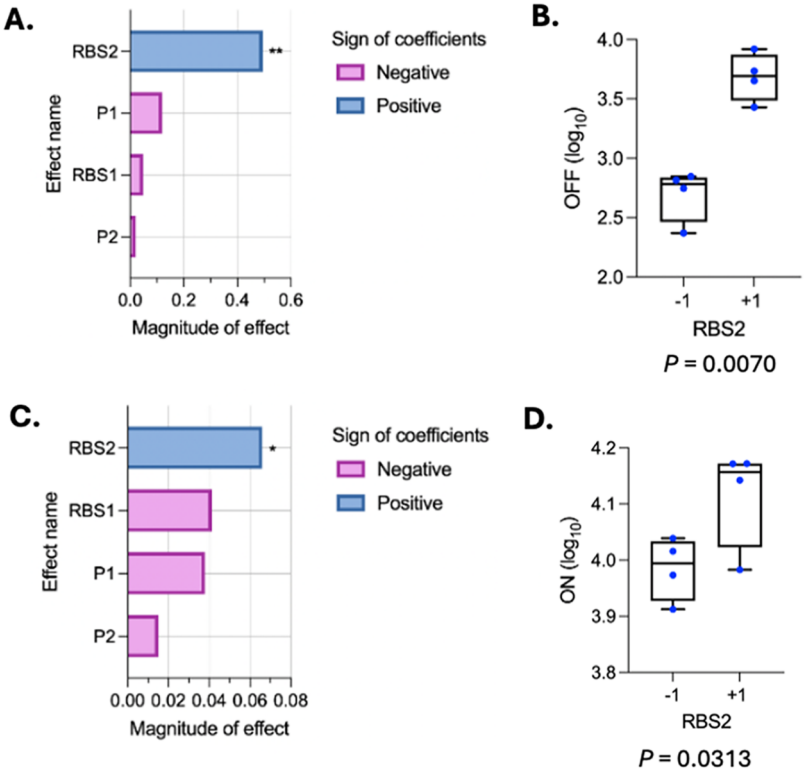

Figure 6. Statistical analysis of RBS2 affecting the dynamic range. (A) Coefficients of model including main effects on the $\log_{10}$-transformed OFF state, *P < 0.05, **P < 0.01. (B) ANOVA analysis of the effect of RBS2 on the $\log_{10}$-transformed OFF state. (C) Coefficients of model including main effects on the $\log_{10}$-transformed ON state. (D) ANOVA analysis of the effect of RBS2 on the $\log_{10}$-transformed ON state.

https://doi.org/10.1021/acssynbio.5c00650
ACS Synth. Biol. 2026, 15, 548−560

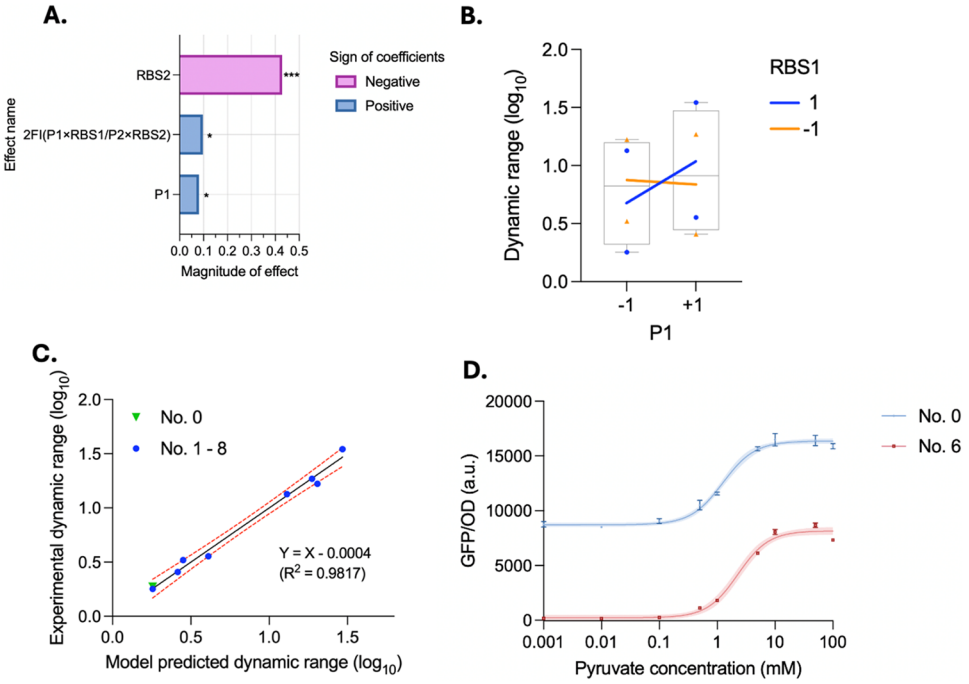

Figure 7. Summary of fractional factorial design results and validation of model prediction. (A) Linear regression analysis of Model 4 ($Y = \beta 0 + \beta 1 \cdot P1 + \beta 2 \cdot RBS2 + \beta 3 \cdot P1 \cdot RBS1$), $^{*}P < 0.05$, $^{***}P < 0.001$. (B) Interaction effects between P1 and RBS1. Blue circles and orange triangles indicate data points under high (1) and low (−1) levels of RBS1, respectively. The lines connect group means and illustrate the interaction effect: under high RBS1 (blue line) and under low RBS1 (orange line). (C) Variant nos. 1−8 (blue dots): correlation between model-predicted and experimentally measured dynamic ranges. The control no. 0 (green triangle) was in 95% CI area. (D) Dose−response curves of control no. 0 and optimized variant no. 6.

Given that RBS2 negatively affects the dynamic range, we further investigated its impact on both OFF and ON states to understand the underlying mechanism. When a strong RBS2 was selected, it significantly impacted both the OFF and ON states, leading to increased leaky expression (Figure 6A,6B and Table S6) and a higher maximum expression level (Figure 6C,D and Table S6). The effect of RBS2 on both the OFF and ON states was significant ($P < 0.05$), particularly in the OFF state, where its influence was more pronounced. The increased translation efficiency driven by RBS2 likely elevated basal expression levels, leading to leaky expression in the OFF state. This leaky expression in the OFF state is particularly critical, as it directly limits the biosensor's dynamic range by raising the signal baseline. Therefore, minimizing RBS2-driven translation in the OFF state is essential for maximizing the dynamic range.

To further understand these effects, we analyzed all interactions between factors (Figure S1). The result showed that the P1 × RBS1 interaction had a greater effect magnitude compared to other interactions. In the resolution IV design, the interaction terms P1 × RBS1 and P2 × RBS2 are aliased, meaning their effects cannot be distinguished statistically (Table S6). Then, we fitted the model using the four main effects and the P1 × RBS1 interaction, which showed that RBS1 and P2 had no significant effect ($P > 0.05$) (Figure S2). We used the AIC for model comparison, and Model 4 ($Y = \beta_0 + \beta_1 \cdot P1 + \beta_2 \cdot RBS2 + \beta_3 \cdot P1 \cdot RBS1$) was selected as the best-performing model (Table S7). In the model, we showed P1 × RBS1 to represent this confounded 2FI. Y represents the predicted $\log_{10}$-transformed dynamic range. According to the final regression coefficients in the linear model, RBS2 negatively impacted the system ($\beta_2 = -0.43$, $P = 0.000075$), while P1 and the P1 × RBS1 interaction contributed positively to the dynamic range ($\beta_1 = 0.081$, $P = 0.034$; $\beta_3 = 0.097$, $P = 0.019$) (Table S6 and Figure 7A). The effect of P1 on the dynamic range was dependent on the level of RBS1 (Figure 7B). When RBS1 was at a high level (1), the dynamic range increased with P1, indicating a positive correlation. At the low level of RBS1 (−1), the dynamic range slightly decreased as P1 increased, showing a weak negative correlation. This suggested that P1 had a notable effect on the dynamic range, and its impact was modulated by RBS1. The interaction of P2 × RBS2 showed the effect of the promoter strength on the dynamic range depends on the level of RBS2 (Figure S3). The proposed regression model demonstrated a good fit with the experimental data, having an adjusted R^2 of 0.98 (Table S6). The relationship between the model-predicted and experimentally observed dynamic ranges for variants 1−8 showed a linear relationship ($R^2 = 0.98$). To further validate the model, strain no. 0 data were projected in the formula, and the result fell within the 95% confidence interval (CI) of the curve (Figure 7C), confirming the accuracy of the model. The linear regression model enabled us to determine the optimal gene expression levels for the genetic circuits' factors, leading to variant no. 6 having 18.54-fold increase in the dynamic range and a 37.22-fold reduction in leaky expression. The Hill's slope of variant no. 0 was 1.57, while that of variant no. 6 was 1.64, indicating a slightly higher response to pyruvate (Figure 7D). These results demonstrate the effectiveness of the linear regression model as a systematic tool for guiding the rational design of regulatory factors to enhance biosensor performance.

2.4. Quantification of Pyruvate in a DoE-Optimized Variant

Based on our linear regression model, variant no. 6 exhibited the highest dynamic range and lowest leaky expression. To evaluate this variant's practical applicability, we quantified

https://doi.org/10.1021/acssynbio.5c00650
ACS Synth. Biol. 2026, 15, 548−560

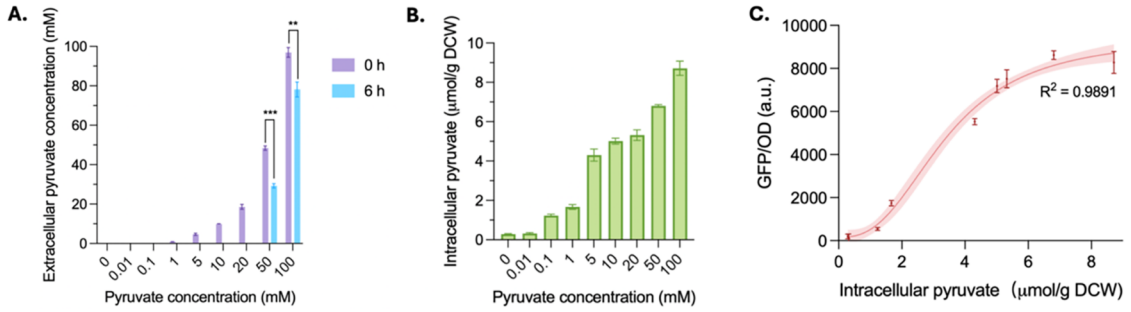

Figure 8. Quantification of extracellular and intracellular pyruvate concentration. (A) Extracellular pyruvate concentration at 0 h (purple column) and 6 h (blue column) after supplementation with 0, 0.01, 1, 5, 10, 20, 50, and 100 mM pyruvate, $^{**}P < 0.01$, $^{***}P < 0.001$. (B) Intracellular pyruvate concentration measured at 6 h. (C) Dose−response curves of the biosensor response to intracellular pyruvate. Data were fitted to a Hill equation (Table S8). The shaded area represents 95% CI.

extracellular and intracellular pyruvate concentration and linked this to biosensor output. Across a range of initial pyruvate concentrations (0−100 mM), we measured extracellular pyruvate concentrations at 0 and 6 h (Figure 8A). At 0 h, the HPLC results confirmed that the measured extracellular concentrations matched the amounts added, down to the detection limit of 0.1 mM. When pyruvate was used as the carbon source, the extracellular concentration decreased by approximately 20 mM after 6 h, indicating pyruvate consumption. Intracellular pyruvate levels increased with rising extracellular concentrations, suggesting pyruvate transport into the cell (Figure 8B). Furthermore, by fitting GFP/OD data as a function of intracellular pyruvate concentrations to the Hill equation, we determined the operational range of 1.23−6.81 μmol/g DCW. This indicated the biosensor had a high sensitivity to pyruvate (Figure 8C). Taken together, these results demonstrated that variant no. 6 is a promising candidate for pyruvate-responsive applications, combining tight gene regulation with high responsiveness.

3. DISCUSSION

The Design−Build−Test−Learn (DBTL) cycle provides a systematic framework to develop and optimize whole-cell biosensors. In this study, we implemented two rounds of DBTL to optimize a PdhR-based pyruvate biosensor in *E. coli*. We systematically screened combinations of promoters and RBSs using a fractional factorial design and identified the key factors affecting biosensor behavior. We developed a PdhR-based pyruvate biosensor that can respond to 0.05−10 mM pyruvate and drastically increased the dynamic range by 18.54-fold and decreased leaky expression by 37.22-fold. The operational intracellular pyruvate range of the DoE-optimized variant was quantified as 1.23−6.81 μmol/g DCW. Previously developed PdhR-based biosensors developed by Wang et al. in *Candida glycerinogenes* responded to 18.2−272.5 mM pyruvate, with dynamic range at approximately 3.5, corresponding to the intracellular concentration range of 0.9−4.2 μmol/g DCW.[37] Xu et al. also reported a pyruvate-responsive genetic circuit in *Bacillus subtilis* that responded to 45.5−181.8 mM pyruvate, with a dynamic range of approximately 4.[32] In comparison, the pyruvate biosensor developed in this study exhibited a broader dynamic range and higher sensitivity at lower extracellular pyruvate concentrations. These differences in the response range and intracellular concentrations reflect host-specific differences in pyruvate metabolism, emphasizing the significance of choosing the appropriate chassis for biosensor design and application.

To achieve this improved biosensor performance and characterize the factors contributing to its performance, we proposed resolution IV design as a suitable balance between information gain and experimental effort, making it a good option to screen the effect of factors in the response.[23] Our approach employed a four-factor, two-level fractional factorial design that successfully identified key regulatory factors and potential interactions. Compared to the three-factor, three-level optimization employed by Berepiki et al.,[38] our method provided greater efficiency with fewer experimental runs and demonstrated the power of statistical modeling in guiding biosensor engineering. Although biosensor responses are inherently nonlinear and follow a sigmoidal Hill curve, our work shows the possibility of fitting linear models to this behavior by focusing on the Hill curve parameters. Expressing the dynamic range as the ratio of ON to OFF levels quantifies the fold change between ON and OFF, rather than characterizing the entire response curve. As such, it is possible for the ON/OFF ratio to be used as a linear performance indicator. This approach allows for effective comparison and optimization of biosensor performance, regardless of the specific shape of the dose−response curve.

The strength of the RBSs and promoters effectively modulated biosensor output by balancing repression strength and reporter expression levels. The observed effects of RBSs can be attributed to their role in controlling translational efficiency, which in turn influences protein abundance and folding.[16] High expression of PdhR due to a strong RBS1 resulted in enhanced repression, reducing the signal span. Similarly, RBS2 was found to significantly influence the dynamic range by modulating both basal (OFF) and maximum (ON) expression. When RBS2 was at a high level, it led to a higher leaky expression as well as increased maximum expression, while a low translation rate reduces both leaky expression and also maximum expression.[39] Since dynamic range is defined as the ratio between maximum and leaky expression of the reporter, a weaker RBS2 lowered the translation rate, which resulted in improved biosensor performance. These effects are consistent with the role of RBSs in determining the translational efficiency and thereby protein abundance.[40] Strong RBSs facilitate protein translation but could result in more mis- and unfolding proteins, whereas weak RBSs slow down protein translation but benefit protein folding.[41] Wang et al. demonstrated that varying the RBS strength can linearly tune protein expression at steady state,[42] and Hoffmann et al. proved that GFP fluorescence correlates well with protein levels measured by Western blotting.[43] Thus,

https://doi.org/10.1021/acssynbio.5c00650
ACS Synth. Biol. 2026, 15, 548−560

the reduced fluorescence that we observed with the weaker RBS2 variant is very likely to reflect lower sfGFP protein expression, particularly in the OFF state. This indicated that adjusting the RBS strength was a simple yet effective strategy to modulate translation rates and thereby optimize biosensor behavior.[41] In addition, P1 significantly affected the dynamic range, highlighting that transcription level control of the PdhR modulates repression strength and output variability. Future optimization efforts can be guided by different objectives. When the goal is to further optimize the dynamic range within the current design space, the most significant factor RBS2 can be fixed at its optimal level (e.g, RBS2 at −1 level), while another significant factor P2 can be further fine-tuned (e.g, intermediate values between −1 and +1) to explore nonlinear responses. Alternatively, factors with the most important main effects could be further optimized by moving outside of the initial design space. For example, a weaker RBS2 and a stronger P2 than currently implemented could be considered to explore whether the dynamic range can be improved further. Overall, these results demonstrated rational tuning of genetic circuits can fine-tune biosensor performance, and statistical modeling can capture meaningful mechanistic relationships within a transcription-factor-based genetic circuit.

The accumulation of endogenous pyruvate in LB medium may further activate the biosensor, preventing complete repression and thereby reducing the contrast between the ON and OFF states. This highlights the need to evaluate the sensor performance under more realistic conditions. Unlike defined media with a precise pyruvate concentration, real-world environments often contain background metabolites that may induce unintended activation, particularly in the presence of carbohydrates. Pyruvate biosensor variant no. 6 responded to other substrates such as glucose, xylose, and acetate (Figure S4A), with glucose eliciting the strongest activation. This is consistent with the fact that these carbon sources are metabolically converted to pyruvate. Bi et al. developed a single-cell pyruvate fluorescence resonance energy transfer (FRET) biosensor to measure dynamic fluctuations in the metabolic network of *E. coli*; they found rapid conversion of glucose to pyruvate occurs on the time scale of second. Moreover, this FRET biosensor can also respond to fructose, acetate, and glycerol.[44] Yang et al. verified PdhR specificity in vitro when developing a pyruvate biosensor in *Saccharomyces cerevisiae*. This study demonstrated that PdhR exhibits high selectivity for pyruvate, with no detectable response observed toward other metabolites such as glucose, fructose, glycerol, PEP, malate, citrate, or succinate. These findings indicate that purified PdhR directly recognizes pyruvate while excluding other central carbon intermediates. When expressed in vivo, their biosensor showed that glucose and fructose activate cytoplasmic pyruvate levels more effectively than direct exposure to pyruvate and that they do so in a dose-dependent manner.[33] This reinforces that the PdhR-based pyruvate biosensor remains molecularly specific, but in living cells, the output also integrates upstream metabolic routing that modulates the intracellular pyruvate level. Together, these results suggest that the metabolic environment may play a crucial role in shaping the pyruvate biosensor performance by affecting their basal expression, response dynamic range, and response speed.

Building on these findings, we considered the structural specificity of our biosensor toward other keto acids. Four additional keto acids were examined: the α-keto acids oxaloacetate (OAA) and α-ketoglutarate (AKG) from the TCA cycle, glyoxylate (GLX) from the glyoxylate shunt, and γ-keto acid levulinic acid. The biosensor responded to OAA and AKG, but not to glyoxylate or levulinic acid (Figure S4). However, OAA is chemically unstable and readily decarboxylates or is metabolically converted back to phosphoenolpyruvate (PEP) and then pyruvate.[45,46] Similarly, AKG can be converted metabolically into pyruvate via the central carbon metabolism.[47] By contrast, glyoxylate requires condensation with acetyl-CoA (via malate synthase) before entering pathways leading to pyruvate,[48] and levulinic acid has no known metabolic route to pyruvate in *E. coli*.[49] These considerations indicate that the biosensor remains specific to pyruvate at the molecular recognition level but its in vivo responses may also reflect indirect activation through rapid metabolic conversions. Future studies involving ligand docking, molecular dynamics simulations, or purified binding assays will be valuable to further quantify affinity differences and refine the mechanistic basis of PdhR specificity.

This optimized biosensor could also provide a versatile platform for metabolic engineering. First, it may act as a dynamic valve for controlling pyruvate flux in synthetic pathways, improving yields of pyruvate-derived compounds such as succinate or alanine.[30,50] Second, it shows potential as a high-throughput screening tool to identify pyruvate-accumulating strains or regulatory mutations.[51] Finally, the modular structure of the biosensor allows for further customization, including the integration of AI-designed synthetic TFs to expand responsiveness to pyruvate analogues.[52−54]

Overall, this work demonstrates how systematic implementation of DBTL cycles guided by statistical modeling such as DoE and AIC, which could enhance biosensor performance, provides a foundation for broader application in synthetic biology circuit design and precision metabolic engineering.

4. METHODS

4.1. Strains and Media

All strains used in this study are listed in Table S1. *E. coli* DH5α was used for cloning, DNA assembly, and plasmid construction. *E. coli* BW25113 Δ*pdhR* was used for biosensor performance assays. Strains were cultured in Lysogeny broth (LB) medium (10 g/L tryptone, 10 g/L NaCl, and 5 g/L yeast extract) with antibiotics. Pyruvate biosensor performance was tested in M9 minimal medium (3.88 g/L K_2HPO_4, 1.63 g/L NaH_2PO_4, 2 g/L $(NH_4)SO_4$, 0.01 g/L EDTA, 0.1 g/L $MgCl_2{\cdot}6H_2O$, 0.002 g/L $ZnSO_4{\cdot}7H_2O$, 0.001 g/L $CaCl_2{\cdot}2H_2O$, 0.005 g/L $FeSO_4{\cdot}7H_2O$, 0.0002 g/L $Na_2MoO_4{\cdot}2H_2O$, 0.0002 g/L $CuSO_4{\cdot}5H_2O$, 0.0004 g/L $CoCl_2{\cdot}6H_2O$, 0.001 g/L $MnCl_2{\cdot}2H_2O$) with ampicillin (100 μg/mL) and kanamycin (50 μg/mL). Sodium pyruvate stock solutions were prepared in Milli-Q H_2O and filtered (0.20 μm) before use.

4.2. Construction of Biosensor and Transformation in *E. coli* Δ*pdhR* Strain

All plasmids used or constructed in this study are listed in Table S2, and all genetic parts, sequences, and primers are listed in Tables S3 and S5. The *pdhR* gene and its promoter P_{pdh} used in the PdhR-based pyruvate biosensor were derived from *E. coli* MG1655. The *pdhR* gene was cloned from the *E. coli* genome by Q5 polymerase (NEB, #M0491S). The pUC19 plasmid containing the ColE origin and ampicillin resistance marker was used as the vector. The constitutive promoter of *pdhR* gene and RBSs were obtained from the iGEM Parts Registry (https://parts.igem.org/Promoters). DNA oligonucleotides and fragments containing promoters and RBS were synthesized by IDT. Fragments were assembled into pUC19 via HiFi DNA Assembly (NEB, #E2621) following manufacturer's protocols. PCR products

https://doi.org/10.1021/acssynbio.5c00650
ACS Synth. Biol. 2026, 15, 548−560

were treated with DpnI (NEB, no. R0176S) to remove methylated template DNA following manufacturer's protocols. All constructs were verified by colony PCR with Phire II polymerase (Thermo Fisher, #F126S) following manufacturer's protocols. PCR positive clones were subsequently validated by Sanger sequencing. Then, electroporation was used to introduce plasmids containing the designed genetic circuits into the KEIO collection, kanamycin-resistant Δ*pdhR* strain[55] (Table S1). Cells were electroporated using a Gene Pulser Xcell electroporator (Bio-Rad) following bacterial standard preset protocols (2.5 kV, 0.1 cm cuvette). Following electroporation, cells were recovered in SOC medium (Super Optimal broth with Catabolite repression, 20 g/L tryptone, 5 g/L yeast extract, 0.584 g/L NaCl, 0.186 g/L KCl, 2.033 g/L $MgCl_2{\cdot}6H_2O$, 2.465 g/L $MgSO_4{\cdot}7H_2O$, and 3.603 g/L glucose 3.603 g/L) at 37 °C for 1 h to allow for plasmid expression. Transformants were then selected on LB agar plates containing kanamycin (50 μg/mL) and ampicillin (100 μg/mL) to ensure the presence of both the genomic kanamycin resistance gene and the ampicillin-resistant plasmid. Transformants were screened by colony PCR using two sets of primers: one set of primers (verify_PG_fwd and verify_PG_rev) to verify correct construct integration of *pdhR* and *sfGFP* in plasmids and another set of primers (verify_PdhR_fwd and verify_PdhR_rev) to confirm *pdhR* gene knockout in *E. coli* Δ*pdhR* strain. Positive clones were further validated by Sanger sequencing and stored at −70 °C in glycerol stocks.

4.3. Biosensor Performance Testing

Biosensor performance was tested by evaluating the GFP production in response to varying pyruvate concentrations. Bacterial strains were streaked from glycerol stocks onto LB agar plates containing ampicillin (100 μg/mL) and kanamycin (50 μg/mL) and incubated overnight at 37 °C. Colonies were inoculated into LB medium with antibiotics and cultured overnight at 37 °C with shaking at 250 rpm. The following morning, 0.5 mL of the overnight culture was diluted into 4.5 mL of fresh LB medium with the antibiotics and grown for 6 h to control background expression. Cells were washed twice with M9 minimal medium and cultured overnight in M9 with antibiotics. After washing once with M9, the cultures were diluted to an initial OD_{600} of 0.3. Pyruvate was added at final concentrations of 0, 0.001, 0.01, 0.1, 0.5, 1, 5, 10, 50, and 100 mM. A total of 150 μL of the culture was transferred to each well of a 96-well plate, covered with 50 μL of mineral oil to prevent evaporation, and incubated at 37 °C with shaking at 731 cpm (2 mm orbit) for 6 h. Fluorescence intensity (sfGFP, excitation at 485 nm; emission at 530 nm) and optical density (OD_{600}) were measured by using a microplate reader (BioTek Synergy H1). Biomass growth was accounted for by normalizing the GFP expression to OD_{600}. Background fluorescence of the strain was corrected by subtracting the GFP/OD values of the negative control (E. coli Δ*pdhR* strain). There was no significant difference between *E. coli* Δ*pdhR* pUC19 and *E. coli* Δ*pdhR* (Figure S5). Therefore, we used *E. coli* Δ*pdhR* as the negative control.

4.4. Biosensor Performance Optimization

For biosensor performance optimization, we used the fractional factorial design of resolution IV. Four factors were considered: (1) P1: a constitutive promoter of *pdhR*, (2) RBS1: a ribosome-binding site controlling the translation efficiency of *pdhR*, (3) P2: a hybrid promoter controlling *sfGFP* transcription, and (4) RBS2: a ribosome-binding site regulating the translation efficiency of *sfGFP*. Each factor was tested at two levels: a high level (coded as +1) and a low level (coded as −1), resulting in a design with $2^{4-1} = 8$ experimental runs. The constitutive promoters and RBSs were obtained from the iGEM Parts Registry. The promoter of PdhR, a strong P_{J108} functioned as 1, while a weak P_{J115} acted as −1. For the hybrid promoter of GFP, the strong $P_{J106\_PdhR\ box}$ was 1, and the weak $P_{J114\_PdhR\ box}$ was −1. To encode promoter levels in the design, we used their experimentally determined activity values reported in the iGEM Parts Registry. According to Registry ranking, P_{J114}, P_{J115}, P_{J106}, and P_{J108} exhibit promoter strengths of 256, 387, 1185, and 1303 au, respectively (Figure S6A). The hybrid promoters contained the PdhR box sequence ATTGGTAAGACCAAT in the core region of the constitutive promoter.[56] The distance between the PdhR box and the transcription start site "+1" was 11 base pairs.[32] Regarding RBS strength, the two levels were assigned based on Registry reported translation activity. RBS30, which exhibits higher measured strength (0.6), was coded as +1, whereas RBS33, which displays much lower activity (0.01), was coded as −1 (Figure S6B). The fragments containing promoters and RBS were synthesized by IDT and assembled into the pUC19 vector by using HiFi DNA Assembly following manufacturer's protocols. The genetic configuration of constructed circuits and levels of four independent factors are listed in Figure 9.

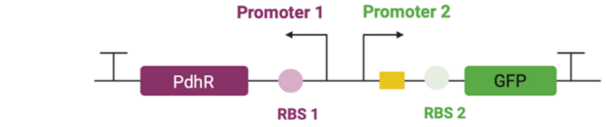

B.

Level	P1	RBS1	P2	RBS2
-1	P_{J115}	RBS33	$P_{J114\_PdhR\ box}$	RBS33
1	P_{J108}	RBS30	$P_{J106\_PdhR\ box}$	RBS30

Figure 9. Genetic configuration of biosensor designs conforming to fractional factorial design. (A) Genetic circuits are shown, and the full table can be found in Table 1. (B) Levels of four independent factors were used in the fractional factorial design. P1 and P2 refer to promoter 1 and promoter 2, respectively. Each factor was tested at two levels: 1 was a high level, while −1 represents a low level.

4.5. Quantification of Pyruvate

To evaluate the sensing performance and establish the correlation between biosensor output and actual pyruvate level, both extracellular and intracellular pyruvate concentration were quantified. For extracellular pyruvate detection, samples were centrifuged at 8000 rpm for 5 min, and the supernatant was measured by ICS-5000 high-performance liquid chromatography (HPLC) with an Aminex HPX-87H column. A 2 mM H_2SO_4 solution was used as an eluent at a flow rate of 0.6 mL/min and column oven temperature of 60 °C. Pyruvate was detected on an ultraviolet (UV) detector at 210 nm and quantified based on an external standard of sodium pyruvate. Intracellular pyruvate was analyzed by first breaking cells using a methanol−water solution and three freeze−thaw cycles.[57] Briefly, 1 mL cells were harvested by centrifugation at 8000 rpm for 5 min, washed twice with cold 0.9% (w/v) sodium chloride to remove extracellular pyruvate, and resuspended in 1 mL of prechilled methanol−water (50:50, v/v) solution at −20 °C. Cells were disrupted by three freeze−thaw cycles (freezing in −70 °C freezer for 30 min and thawing on ice for 4 min with 1 min of vortexing). The lysate was centrifuged at 14,000 rpm for 10 min, and the supernatant containing intracellular pyruvate was collected. After this process, methanol was evaporated in a vacuum centrifuge (Concentrator Plus, Eppendorf) at 45 °C under the V-AQ model for 2 h. After evaporation, 10 μL of Milli-Q water was added to dissolve samples thoroughly and subsequently analyzed using the pyruvate assay kit (MAK332) following manufacturer's protocols. To account for biomass variation, the intracellular pyruvate concentration was normalized by dry cell weight (DCW). DCW was estimated based on a previously established calibration curve correlating OD_{600} to DCW (Figure S7).

4.6. Data Processing and Modeling

All measurements were performed in triplicate. For pairwise comparisons between two independent groups, a *t* test was performed using the T.TEST function in Microsoft Excel 16.80, and statistical significance is indicated as $^*P < 0.05$, $^{**}P < 0.01$, and $^{***}P < 0.001$.

Responses of the biosensors were obtained by fitting the experimental data to the Hill equation (Figure 1A)

https://doi.org/10.1021/acssynbio.5c00650
ACS Synth. Biol. 2026, 15, 548−560

$$y = \mathrm{OFF} + (\mathrm{ON} - \mathrm{OFF})\frac{x^n}{K^n + x^n} \quad (1)$$

where y is the relative fluorescence intensity (GFP/OD), ON/OFF is the maximum/minimum relative fluorescence intensity, x is the concentration of pyruvate, K is the threshold of the gene circuit, and n is the Hill coefficient. Parameter estimation and Hill equation visualization were performed in GraphPad Prism 10.

The fractional factorial design form was designed with JMP Pro 17 software. Statistical data was performed by R version 4.3.2. The linear model was fit using the lm function, and the Pareto plots were generated with the R paretoPlot functions.[58] The relationship between the responses and factors was expressed by the linear regression equation

$$Y = \beta_0 + \sum_{i=1}^{n} \beta_i X_i + \sum_{i=1}^{n} \sum_{j=i+1}^{n} \beta_{ij} X_i X_j \quad (2)$$

where Y represents the predicted response, X_i are the considered factors, β_0 is the interception coefficient, β_i is the linear coefficient of the main effect (ME), and β_{ij} is the coefficient of the two-factor interactions (2FI). The quality of the regression equations was assessed according to the adjusted coefficient of determination (Adj R^2). Statistical analysis of the model was performed using analysis of variance (ANOVA) and $P < 0.05$ was considered significant, and statistically significant is indicated as $^*P < 0.05$, $^{**}P < 0.01$, and $^{***}P < 0.001$.

The quality of the regression models was evaluated by using the Akaike Information Criterion (AIC), which balances model fit and complexity. The Akaike equation (AIC formula) is as follows

$$\mathrm{AIC} = 2K - 2\ln(\hat{L}) \quad (3)$$

where K represents the number of estimated parameters in the model and $\hat{L}$ is the maximized value of the likelihood function. AIC values are calculated using the AIC function in R version 4.3.2.

For pairwise comparisons between two groups, an unpaired two-tailed Welch's t test was used to evaluate statistical significance, assuming unequal variances.

Schematic illustrations were created with BioRender (BioRender.com).

■ ASSOCIATED CONTENT

Data Availability Statement

Data will be made available upon reasonable request.

Supporting Information

The Supporting Information is available free of charge at https://pubs.acs.org/doi/10.1021/acssynbio.5c00650.

Additional experimental details, materials, and methods, including strains and plasmids used in this study; genetic parts and DNA sequences; primer lists; regression statistics and model comparison; best-fit parameters for biosensor dose−response curves; regression analyses; and interaction effects, specificity of pyruvate biosensor, and dry cell weight calibration curves (PDF)

■ AUTHOR INFORMATION

Corresponding Author

Pieter Candry − *Laboratory of Systems and Synthetic Biology, Wageningen University & Research, 6708 WE Wageningen, The Netherlands;* orcid.org/0000-0002-7784-3650; Email: pieter.candry@wur.nl

Authors

Zihan Gao − *Laboratory of Systems and Synthetic Biology, Wageningen University & Research, 6708 WE Wageningen, The Netherlands;* orcid.org/0009-0005-0470-5723

Maria Suarez-Diez − *Laboratory of Systems and Synthetic Biology, Wageningen University & Research, 6708 WE Wageningen, The Netherlands;* orcid.org/0000-0001-5845-146X

Complete contact information is available at: https://pubs.acs.org/10.1021/acssynbio.5c00650

Author Contributions

Z.G. performed the experiments, analyzed the results, and wrote the initial draft. P.C. and M.S.D. guided the experimental design and data analysis. All authors contributed to writing and reviewing the manuscript.

Notes

The authors declare no competing financial interest.

■ ACKNOWLEDGMENTS

The authors acknowledge the assistance of Dr. Zeynep Efsun Duman-Özdamar for valuable guidance of data analysis, Dr. Enrique Asin-Garcia for strain selection and helpful discussions, and Silvia Rodríguez Marcos for experiment material support. Zihan Gao was supported by the China Scholarship Council (CSC) under Grant No. 202304910065. Pieter Candry was supported by the Dutch Research Council (NWO) Veni Talent Programme (File No. 21027) and the Dutch Sectorplan Bèta-II—Biology. Figures 1,2, and 3A were created with BioRender (BioRender.com). Figure 1C fractional factorial design matrix was adapted from Kevin Dunn's DoE teaching materials (Dunn, 2025).

■ REFERENCES

(1) Morales, M. A.; Halpern, J. M. Guide to Selecting a Biorecognition Element for Biosensors. *Bioconjugate Chem.* **2018**, *29*, 3231−3239.

(2) van der Meer, J. R.; Belkin, S. Where microbiology meets microengineering: design and applications of reporter bacteria. *Nat. Rev. Microbiol.* **2010**, *8*, 511−522.

(3) Moraskie, M.; Roshid, M. H. O.; O'Connor, G.; Dikici, E.; Zingg, J.-M.; Deo, S.; Daunert, S. Microbial whole-cell biosensors: Current applications, challenges, and future perspectives. *Biosens. Bioelectron.* **2021**, *191*, No. 113359.

(4) Liu, D.; Evans, T.; Zhang, F. Applications and advances of metabolite biosensors for metabolic engineering. *Metab. Eng.* **2015**, *31*, 35−43.

(5) Chiang, A. J.; Hasty, J. Design of synthetic bacterial biosensors. *Curr. Opin. Microbiol.* **2023**, *76*, No. 102380.

(6) Rogers, J. K.; Guzman, C. D.; Taylor, N. D.; Raman, S.; Anderson, K.; Church, G. M. Synthetic biosensors for precise gene control and real-time monitoring of metabolites. *Nucleic Acids Res.* **2015**, *43*, 7648−7660.

(7) Asemoloye, M. D.; Marchisio, M. A. Synthetic metabolic transducers in Saccharomyces cerevisiae as sensors for aromatic permeant acids and bioreporters of hydrocarbon metabolism. *Biosens. Bioelectron.* **2023**, *220*, No. 114897.

(8) Tanniche, I.; Behkam, B. Engineered live bacteria as disease detection and diagnosis tools. *J. Biol. Eng.* **2023**, *17*, No. 65.

(9) Hu, L.; Su, H.; Chen, S.; Chen, X.; Guo, M.; Liu, H.; Yang, H.; Sun, B. Lab in a cell: A bioautomated and biointegrated whole-cell biosensing platform for food hazards analysis. *Trends Food Sci. Technol.* **2024**, *148*, No. 104489.

(10) Wan, X.; Volpetti, F.; Petrova, E.; French, C.; Maerkl, S. J.; Wang, B. Cascaded amplifying circuits enable ultrasensitive cellular sensors for toxic metals. *Nat. Chem. Biol.* **2019**, *15*, 540−548.
(11) Liu, C.; Yu, H.; Zhang, B.; Liu, S.; Liu, C.-g.; Li, F.; Song, H. Engineering whole-cell microbial biosensors: Design principles and applications in monitoring and treatment of heavy metals and organic pollutants. *Biotechnol. Adv.* **2022**, *60*, No. 108019.
(12) Carpenter, A. C.; Paulsen, I. T.; Williams, T. C. Blueprints for Biosensors: Design, Limitations, and Applications. *Genes* **2018**, *9*, No. 375, DOI: 10.3390/genes9080375.
(13) Grömping, U. R Package FrF2 for Creating and Analyzing Fractional Factorial 2-Level Designs. *J. Stat. Software* **2014**, *56* (1), 1−56.
(14) Pham, C.; Stogios, P. J.; Savchenko, A.; Mahadevan, R. Advances in engineering and optimization of transcription factor-based biosensors for plug-and-play small molecule detection. *Curr. Opin. Biotechnol.* **2022**, *76*, No. 102753.
(15) Zhang, C.; Liu, H.; Li, X.; Xu, F.; Li, Z. Modularized synthetic biology enabled intelligent biosensors. *Trends Biotechnol.* **2023**, *41*, 1055−1065.
(16) Faure, G.; Ogurtsov, A. Y.; Shabalina, S. A.; Koonin, E. V. Role of mRNA structure in the control of protein folding. *Nucleic Acids Res.* **2016**, *44*, 10898−10911.
(17) Casamassimi, A.; Ciccodicola, A. Transcriptional Regulation: Molecules, Involved Mechanisms, and Misregulation. *Int. J. Mol. Sci.* **2019**, *20*, No. 1281, DOI: 10.3390/ijms20061281.
(18) Moreno-Paz, S.; van der Hoek, R.; Eliana, E.; Dos Santos, V. A. P. M.; Schmitz, J.; Suarez-Diez, M. Combinatorial optimization of pathway, process and media for the production of p-coumaric acid by Saccharomyces cerevisiae. *Microb. Biotechnol.* **2024**, *17*, No. e14424.
(19) Duman-Özdamar, Z. E.; Dos Santos, V. A. P. M.; Hugenholtz, J.; Suarez-Diez, M. Tailoring and optimizing fatty acid production by oleaginous yeasts through the systematic exploration of their physiological fitness. *Microb. Cell Fact.* **2022**, *21*, No. 228.
(20) Duman-Özdamar, Z. E.; Julsing, M. K.; Verbokkem, J. A. C.; Wolbert, E.; dos Santos, V. A. P. M.; Hugenholtz, J.; Suarez-Diez, M. Model-driven engineering of Cutaneotrichosporon oleaginosus ATCC 20509 for improved microbial oil production. *Bioresour. Technol.* **2025**, *421*, No. 132142.
(21) Xu, P.; Rizzoni, E. A.; Sul, S. Y.; Stephanopoulos, G. Improving Metabolic Pathway Efficiency by Statistical Model-Based Multivariate Regulatory Metabolic Engineering. *ACS Synth. Biol.* **2017**, *6*, 148−158.
(22) Rezende, C. A.; Atta, B. W.; Breitkreitz, M. C.; Simister, R.; Gomez, L. D.; McQueen-Mason, S. J. Optimization of biomass pretreatments using fractional factorial experimental design. *Biotechnol. Biofuels* **2018**, *11*, No. 206.
(23) Moreno-Paz, S.; Schmitz, J.; Suarez-Diez, M. In silico analysis of design of experiment methods for metabolic pathway optimization. *Comput. Struct. Biotechnol. J.* **2024**, *23*, 1959−1967.
(24) Akaike, H. A new look at the statistical model identification. *IEEE Trans. Autom. Control* **1974**, *19*, 716−723.
(25) Chaisupa, P.; Wright, R. C. State-of-the-art in engineering small molecule biosensors and their applications in metabolic engineering. *SLAS Technol.* **2024**, *29*, No. 100113.
(26) Carbonell, P.; Jervis, A. J.; Robinson, C. J.; Yan, C.; Dunstan, M.; Swainston, N.; Vinaixa, M.; Hollywood, K. A.; Currin, A.; Rattray, N. J. W.; Taylor, S.; Spiess, R.; Sung, R.; Williams, A. R.; Fellows, D.; Stanford, N. J.; Mulherin, P.; Le Feuvre, R.; Barran, P.; Goodacre, R.; Turner, N. J.; Goble, C.; Chen, G. G.; Kell, D. B.; Micklefield, J.; Breitling, R.; Takano, E.; Faulon, J. L.; Scrutton, N. S. An automated Design-Build-Test-Learn pipeline for enhanced microbial production of fine chemicals. *Commun. Biol.* **2018**, *1*, No. 66.
(27) Gurdo, N.; Volke, D. C.; McCloskey, D.; Nikel, P. I. Automating the design-build-test-learn cycle towards next-generation bacterial cell factories. *New Biotechnol.* **2023**, *74*, 1−15.
(28) Wang, J.; Zhang, R.; Zhang, Y.; Yang, Y.; Lin, Y.; Yan, Y. Developing a pyruvate-driven metabolic scenario for growth-coupled microbial production. *Metab. Eng.* **2019**, *55*, 191−200.
(29) Hossain, G. S.; Saini, M.; Miyake, R.; Ling, H.; Chang, M. W. Genetic Biosensor Design for Natural Product Biosynthesis in Microorganisms. *Trends Biotechnol.* **2020**, *38*, 797−810.
(30) Noda, S.; Mori, Y.; Fujiwara, R.; Shirai, T.; Tanaka, T.; Kondo, A. Reprogramming *Escherichia coli* pyruvate-forming reaction towards chorismate derivatives production. *Metab. Eng.* **2021**, *67*, 1−10.
(31) Pundir, C. S.; Malik, M.; Chaudhary, R. Quantification of pyruvate with special emphasis on biosensors: A review. *Microchem. J.* **2019**, *146*, 1102−1112.
(32) Xu, X.; Li, X.; Liu, Y.; Zhu, Y.; Li, J.; Du, G.; Chen, J.; Ledesma-Amaro, R.; Liu, L. Pyruvate-responsive genetic circuits for dynamic control of central metabolism. *Nat. Chem. Biol.* **2020**, *16*, 1261−1268.
(33) Yang, L.; Jia, C.; Xie, B.; Chen, M.; Cheng, X.; Chen, X.; Dong, W.; Zhou, J.; Jiang, M. Lighting up Pyruvate Metabolism in Saccharomyces cerevisiae by a Genetically Encoded Fluorescent Biosensor. *J. Agric. Food Chem.* **2024**, *72*, 1651−1659.
(34) Ogasawara, H.; Ishida, Y.; Yamada, K.; Yamamoto, K.; Ishihama, A. PdhR (pyruvate dehydrogenase complex regulator) controls the respiratory electron transport system in *Escherichia coli*. *J. Bacteriol.* **2007**, *189*, 5534−5541.
(35) Quail, M. A.; Guest, J. R. Purification, characterization and mode of action of PdhR, the transcriptional repressor of the pdhR-aceEF-lpd operon of *Escherichia coli*. *Mol. Microbiol.* **1995**, *15*, 519−529.
(36) Göhler, A.-K.; Kökpinar, Ö.; Schmidt-Heck, W.; Geffers, R.; Guthke, R.; Rinas, U.; Schuster, S.; Jahreis, K.; Kaleta, C. More than just a metabolic regulator–elucidation and validation of new targets of PdhR in *Escherichia coli*. *BMC Syst. Biol.* **2011**, *5*, No. 197.
(37) Wang, X.; Zhao, C.; Lu, X.; Zong, H.; Zhuge, B. Balancing Pyruvate Node Based on a Dual-Layered Dynamic Regulation System to Improve the Biosynthesis of Caffeic Acid in Candida glycerinogenes. *J. Agric. Food Chem.* **2023**, *71*, 8981−8990.
(38) Berepiki, A.; Kent, R.; Machado, L. F. M.; Dixon, N. Development of High-Performance Whole Cell Biosensors Aided by Statistical Modeling. *ACS Synth. Biol.* **2020**, *9*, 576−589.
(39) Rubens, J. R.; Selvaggio, G.; Lu, T. K. Synthetic mixed-signal computation in living cells. *Nat. Commun.* **2016**, *7*, No. 11658.
(40) Levin-Karp, A.; Barenholz, U.; Bareia, T.; Dayagi, M.; Zelcbuch, L.; Antonovsky, N.; Noor, E.; Milo, R. Quantifying translational coupling in *E. coli* synthetic operons using RBS modulation and fluorescent reporters. *ACS Synth. Biol.* **2013**, *2*, 327−336.
(41) Ding, N.; Yuan, Z.; Zhang, X.; Chen, J.; Zhou, S.; Deng, Y. Programmable cross-ribosome-binding sites to fine-tune the dynamic range of transcription factor-based biosensor. *Nucleic Acids Res.* **2020**, *48*, 10602−10613.
(42) Wang, B.; Kitney, R. I.; Joly, N.; Buck, M. Engineering modular and orthogonal genetic logic gates for robust digital-like synthetic biology. *Nat. Commun.* **2011**, *2*, No. 508.
(43) Hoffmann, S. A.; Cai, Y. Engineering stringent genetic biocontainment of yeast with a protein stability switch. *Nat. Commun.* **2024**, *15*, No. 1060.
(44) Bi, S.; Kargeti, M.; Colin, R.; Farke, N.; Link, H.; Sourjik, V. Dynamic fluctuations in a bacterial metabolic network. *Nat. Commun.* **2023**, *14*, No. 2173.
(45) Jetten, M. S. M.; Sinskey, A. J. Purification and properties of oxaloacetate decarboxylase from Corynebacterium glutamicum. *Antonie van Leeuwenhoek* **1995**, *67*, 221−227.
(46) Koendjbiharie, J. G.; van Kranenburg, R.; Kengen, S. W. M. The PEP-pyruvate-oxaloacetate node: variation at the heart of metabolism. *FEMS Microbiol Rev.* **2021**, *45*, No. fuaa061, DOI: 10.1093/femsre/fuaa061.
(47) Gray, L. R.; Tompkins, S. C.; Taylor, E. B. Regulation of pyruvate metabolism and human disease. *Cell. Mol. Life Sci.* **2014**, *71*, 2577−2604.
(48) Singh, V. K.; Ghosh, I. Kinetic modeling of tricarboxylic acid cycle and glyoxylate bypass in Mycobacterium tuberculosis, and its application to assessment of drug targets. *Theor. Biol. Med. Modell.* **2006**, *3*, No. 27.

(49) Rand, J. M.; Pisithkul, T.; Clark, R. L.; Thiede, J. M.; Mehrer, C. R.; Agnew, D. E.; Campbell, C. E.; Markley, A. L.; Price, M. N.; Ray, J.; Wetmore, K. M.; Suh, Y.; Arkin, A. P.; Deutschbauer, A. M.; Amador-Noguez, D.; Pfleger, B. F. A metabolic pathway for catabolizing levulinic acid in bacteria. *Nat. Microbiol.* **2017**, *2*, 1624−1634.
(50) Batianis, C.; van Rosmalen, R. P.; Major, M.; van Ee, C.; Kasiotakis, A.; Weusthuis, R. A.; dos Santos, V. A. P. M. A tunable metabolic valve for precise growth control and increased product formation in Pseudomonas putida. *Metab. Eng.* **2023**, *75*, 47−57.
(51) Moxley, W. C.; Eiteman, M. A. Pyruvate Production by *Escherichia coli* by Use of Pyruvate Dehydrogenase Variants. *Appl. Environ. Microbiol.* **2021**, *87*, No. e0048721.
(52) Zhang, Z.; Shen, W. X.; Liu, Q.; Zitnik, M. Efficient generation of protein pockets with PocketGen. *Nat. Mach. Intell.* **2024**, *6*, 1382−1395.
(53) Baek, M.; McHugh, R.; Anishchenko, I.; Jiang, H.; Baker, D.; DiMaio, F. Accurate prediction of protein−nucleic acid complexes using RoseTTAFoldNA. *Nat. Methods* **2024**, *21*, 117−121.
(54) Teukam, Y. G. N.; Dassi, L. K.; Manica, M.; Probst, D.; Schwaller, P.; Laino, T. Language models can identify enzymatic binding sites in protein sequences. *Comput. Struct. Biotechnol. J.* **2024**, *23*, 1929−1937.
(55) Baba, T.; Ara, T.; Hasegawa, M.; Takai, Y.; Okumura, Y.; Baba, M.; Datsenko, K. A.; Tomita, M.; Wanner, B. L.; Mori, H. Construction of *Escherichia coli* K-12 in-frame, single-gene knockout mutants: the Keio collection. *Mol. Syst. Biol.* **2006**, *2*, No. 2006-0008.
(56) Anzai, T.; Imamura, S.; Ishihama, A.; Shimada, T. Expanded roles of pyruvate-sensing PdhR in transcription regulation of the *Escherichia coli* K-12 genome: fatty acid catabolism and cell motility. *Microb. Genomics* **2020**, *6*, No. e000442, DOI: 10.1099/mgen.0.000442.
(57) Smart, K. F.; Aggio, R. B.; Van Houtte, J. R.; Villas-Bôas, S. G. Analytical platform for metabolome analysis of microbial cells using methyl chloroformate derivatization followed by gas chromatography-mass spectrometry. *Nat. Protoc.* **2010**, *5*, 1709−1729.
(58) Team, R. C. *R: A Language and Environment for Statistical Computing*. 2023.

https://doi.org/10.1021/acssynbio.5c00650
ACS Synth. Biol. 2026, 15, 548−560